Dalton Transactions

ROYAL SOCIETY OF CHEMISTRY

PAPER

View Article Online
View Journal | View Issue

Cite this: *Dalton Trans.*, 2026, **55**, 761

Dual-function Ni-based MOF for hydrogen storage and CO_2 to carbonate cyclic catalysis

Elena García-Rojas, [a] Helena Montes-Andrés, [a] Jesús Tapiador, [a] Carmen Martos, *[a] Pablo Salcedo-Abraira, [b] Duane Choquesillo-Lazarte, [c] Gisela Orcajo [a] and Pedro Leo *[a]

International organizations highlight the need for technological progress with minimal environmental impact. In this context, we present Ni-URJC-3, a novel nickel-based metal–organic framework (MOF) with promising performance in H_2 and CO_2 adsorption and as a heterogeneous catalyst for cycloaddition reactions between epoxides and CO_2. The presence of azo groups (–N=N–) in the organic linker enhances both adsorption and catalytic activity, acting as Lewis bases and outperforming other Ni-MOFs, even those with higher surface areas. Ni-URJC-3 exhibits an excellent H_2 gravimetric capacity of 3.7 wt% and a total volumetric uptake of 59.5 g L^{-1}, approaching the U.S. DOE target for hydrogen storage. This is attributed to both chemical factors, such as the electronic effects of azo groups, and physical ones, including the confinement effect within its microporous structure that enhances H_2 framework interactions. Regarding CO_2, the material shows a high adsorption enthalpy of 35.8 kJ mol^{-1} and performs efficiently as a catalyst for the cycloaddition of CO_2 with various epoxides. These results demonstrate the potential of Ni-URJC-3 as a multifunctional MOF for environmental applications, particularly in gas storage and CO_2 transformation, contributing to the design of advanced materials aligned with sustainability goals.

Received 16th September 2025,
Accepted 20th November 2025

DOI: 10.1039/d5dt02218e

rsc.li/dalton

1. Introduction

The production, handling and storage of energy have become fundamental concerns in our present world. According to the international Energy Agency, the proportion of energy consumption accounted for by oil, coal and natural gas currently exceeds 70%.[1] As a consequence of the combustion of fossil fuels, the concentration of CO_2 in the troposphere is rising to a degree that gives rise to serious concerns. These levels are contributing to social alarm and a range of significant environmental issues, including the greenhouse effect and ocean acidification.[2–4] The elevated environmental impact generated by the use of fossil fuels, coupled with the continuous rise in their prices and dependence on oil-producing countries, underscores the need to develop new global, clean and sustainable energy sources. Meanwhile, as these options are being developed, carbon capture and utilization (CCU) technologies should also be employed as complementary strategies to assure a more sustainable energy system.[5,6]

Among the different carbon capture and utilization (CCU) strategies, CO_2 adsorption represents a crucial step, as it enables the efficient retention of this greenhouse gas prior to any chemical transformation. The main challenge is to develop porous materials that combine high uptake capacity, suitable enthalpy of adsorption, and good regenerability, allowing for practical cyclic operation.[7,8] Beyond capture, non-reductive conversion of CO_2 is one of the most promising methods for transforming this atmospheric pollutant, as it enables the reaction to proceed with low energy input, despite the low reactivity of the compound, effectively converting this molecule into value-added chemicals.[9,10] It is evident that there are multiple non-reductive CO_2 conversion pathways capable of yielding organic compounds of significant industrial pertinence. For instance, the cycloaddition of CO_2 with epoxides to form cyclic carbonates can yield products used as electrolytes in lithium-ion batteries, precursors for pharmaceutical intermediates, raw materials for plastics, and environmentally friendly non-protic solvents.[11,12]

Concurrently, interest in hydrogen as an energy carrier is increasing, primarily due to its abundance, high energy density when compared to fossil fuels, and the absence of direct CO_2 emissions.[13] Consequently, hydrogen is regarded as

[a]*Chemical and Environmental Engineering Group, ESCET, Universidad Rey Juan Carlos, C/ Tulipán s/n 28933, Móstoles, Spain. E-mail: pedro.leo@urjc.es; Tel: +34 91 488 83 57*
[b]*Department of Inorganic Chemistry, University of Granada, Avda. Fuentenueva s/n, Granada, Spain*
[c]*Laboratorio de Estudios Cristalográficos, IACT, CSIC-Universidad de Granada, Avda. de las Palmeras 4, 18100 Armilla, Granada, Spain*

a highly prospective "fuel of the future" contingent upon its sustainable production, namely through the utilisation of water *via* renewable energy sources, especially in transportation, power generation, and industrial sectors. This suggests that the next significant transformation in the energy sector regarding the decarbonisation target by 2050 will be based on the hydrogen economy.[14] At present, 100 million tons of hydrogen are produced per annum, with an anticipated increase of approximately 20 million tons by the close of the decade. By 2050, it is projected that production will reach approximately 500 million tons in order to facilitate the decarbonisation process.[15] While the majority of hydrogen is currently produced from natural gas and consumed in close proximity to the production sites,[16] there is an expectation that demand for blue hydrogen (hydrogen produced from hydrocarbons accompanied by CO_2 capture) will increase, representing a crucial step towards a sustainable hydrogen economy.[17]

One of the most important challenges for the hydrogen market progress is the development of efficient hydrogen storage solutions. Existing hydrogen storage technologies, the majority of which are based on cryogenic pressure vessels, are characterised by a number of significant limitations. These include complex thermal management systems, boil-off losses, slow response rates, elevated operating pressures (350–800 bar) and low energy densities. The primary constraints associated with hydrogen are attributable to its high volatility and low density, which significantly complicates its effective storage and transportation.[18,19]

In the domain of storage, the employment of highly porous solid adsorbents has emerged as a particularly promising avenue of investigation.[20] This method has been demonstrated to offer higher deliverable H_2 capacities than simple compression techniques while operating at lower pressures. The United States Department of Energy (DOE) has set that in 2025 the hydrogen storage objective will be 5.5% weight of gravimetric capacity and 40 g L^{-1} of volumetric capacity at ambient temperature and pressure lower than 100 bar.[21,22] To meet these goals, it is imperative to design materials with high deliverable gravimetric and volumetric capacities, reducing the size and weight of the storing devices.[23–25]

In this context, Metal Organic Frameworks (MOFs) have emerged as ideal candidates for the development of next-generation H_2 and CO_2 storage systems and also as materials for CO_2 conversion due to their outstanding properties and unique structural and chemical tunability.[26–29] The affinity of the substrates with MOFs surface can be enhanced through the rational selection of the framework components, thus enabling tailored optimization of the physicochemical properties required for these applications.[30]

For instance, the synthesis of materials with tetratopic organic ligands of carboxylic nature allows for materials with high thermal stability and high porosity.[31] These tetratopic ligands can be qualified as highly symmetric building units,[32] thus facilitating the assembly process of secondary building units, resulting in crystalline structures with large cavities. The ligand 5,5′-(diazene-1,2-diyl)diisophthalic acid (H_4ABTC) presents an interesting coordination chemistry, as its four carboxylic groups can be fully or partially deprotonated, forming H_2ABTC^{2-}, $HABTC^{3-}$, and $ABTC^{4-}$ anions depending on the pH of the synthetic medium, allowing a high diversity of coordination modes with the metal cation. Moreover, the –N=N– functional group can enhance to the interaction between H_2 and CO_2 molecules and the framework due to the presence of its two free electron pairs (one pair for each nitrogen atom) and its ability to behave as a Lewis base.[33] Additionally, the azo group N=N confers to the organic ligand certain conformational flexibility, as it can transition between the *cis* and *trans* states can occur by irradiation.[34] According to literature, the highest H_2 adsorption enthalpies in MOF materials have been observed in structures based on cobalt and nickel.[35,36]

Based on these premises, a new MOF material, has been crystallized using the tetratopic organic ligand 5,5′-(diazene-1,2-diyl) diisophthalic acid (H_4ABTC) as organic linker with the objective of containing structural nickel and azo Lewis acid and basic groups, respectively, and a high coordinated organic ligand for building a robust material. This material has been named Ni-URJC-3 (URJC in reference to the Universidad Rey Juan Carlos) and tested as H_2 and CO_2 adsorbent and catalyst in CO_2 chemical transformation to validate its chemical and physical properties.

2. Experimental

All analytical reagents were commercial products, and they were used without further purification.

2.1. Synthesis of 5,5′-(diazene-1,2-diyl)diisophthalic acid (H_4ABTC)

The H_4ABTC ligand is not commercially available; therefore it was synthesised in the laboratory with a 79% yield by a one-step synthetic route based on the selective reduction of the nitro group of the 5-nitroisophthalic acid.[37] A detailed description of the synthesis process is provided in the SI.

Synthesis of Ni-URJC-3. In a typical synthesis, 35.8 mg (0.01 mmol) of H_4ABTC and 29 mg (0.01 mmol) of nickel(II) nitrate hexahydrate were dissolved in a mixture of *N*,*N*′-dimethylformamide (DMF) (5 mL) and nitric acid (75 μL). The solution was added to a 20 mL scintillation vial and placed in a preheated oven at 120 °C for 72 hours. Then, goldish crystals were isolated by decanting the mother liquor and washed with DMF. The crystals were of a suitable size for single X-ray diffraction. The synthesis yield was *ca.* 58% based on the linker content. IR = 1656 (m), 1616 (s), 1552 (s), 1441 (s), 1377 (m), 1243 (m), 1105 (s), 920 (s), 776 (s), 715 (s), 681 (s), 514 (m) cm^{-1}. Anal. cal. for $C_{32.7}H_{39.8}N_{7.6}Ni_2O_{13.6}$: C, 44.9; H, 4.6; N, 12.2. Found C, 44.1; H, 4.8; N, 11.7.

2.2. Characterization techniques

The crystalline structure of Ni-URJC-3 was determined through single-crystal X-ray diffraction analysis. For this, selected single crystals were carefully mounted on a mitogen support and analyzed using a Bruker D8 VENTURE diffractometer, which fea-

tures a CCD area detector and graphite-monochromated Mo-Kα radiation (λ = 0.71073 Å). X-ray diffraction data acquisition was performed employing the ω-scan strategy. The collected data were processed and reduced using the APEX3 software package,[38] with absorption corrections applied *via* SADABS. The crystal structure was determined using intrinsic methods with SHELXT and refined through full-matrix least squares fitting on F^2, incorporating all observed reflections and employing anisotropic displacement parameters.[39] For visualization and structural refinement, the OLEX2 graphical interface was utilized.[40] Hydrogen atoms were modeled as riding on their respective bonded atoms, with isotropic thermal displacement factors set at 1.2 or 1.5 times those of their parent atoms, depending on the organic ligand environment.

During the refinement process, electron density regions corresponding to highly disordered DMF molecules were identified. The presence of 2.5 DMF molecules was accounted for in the empirical formula, ensuring an accurate determination of calculated density, absorption coefficient, and molecular weight. Additionally, Ni-URJC-3 was found to exhibit inversion twinning. A summary of the structure determination and refinement parameters is provided in Tables S1 and S2. The crystallographic dataset (excluding structure factors) for this compound has been deposited in the Cambridge Crystallographic Data Centre (CCDC) under deposition number CCDC 2391335.

Powder X-ray diffraction (XRD) patterns were recorded using a PHILIPS X'PERT diffractometer equipped with CuKα radiation (1.54056 Å), scanning over a 2θ range of 5 to 50° with a resolution of 0.01°. The textural properties were examined through argon adsorption–desorption isotherms at −186 °C, measured with an AutoSorb system (Quantachrome Instruments). Prior to analysis, the samples were subjected to *in situ* evacuation under high vacuum (<10^{-7} bar) for 12 h at 120 °C to ensure complete removal of physisorbed species. The surface area was estimated using the Brunauer–Emmett–Teller (BET) model,[41] while pore volume and pore size distribution were determined *via* non-local density functional theory (NLDFT) calculations, assuming an Ar adsorption kernel at −186 °C on a carbon surface with cylindrical pores (NLDFT equilibrium model).[42] Thermal stability and decomposition behavior were evaluated through simultaneous thermogravimetric analysis (TGA) and derivative thermogravimetric (DTG) measurements, performed under an air atmosphere (100 mL min^{-1}) at a controlled heating rate of 5 °C min^{-1} up to 900 °C, using a Mettler Toledo TGA/DSC1 instrument. Elemental composition was determined using a Flash 2000 analyzer (Thermo Fisher Scientific), which operates with a thermal conductivity detector (TCD). The quantification of carbon, nitrogen, and hydrogen was conducted through oxidation/reduction reactions in a furnace maintained at 900 °C, whereas oxygen content was determined in a dedicated pyrolysis reactor heated to 1060 °C. Scanning electron microscopy (SEM) images were obtained using a TM1000-Hitachi microscope, operating at an accelerating voltage of 15 kV. Additionally, ^{1}H NMR and ^{13}C NMR spectra were recorded on a Varian Mercury Plus 400 MHz spectrometer, employing tetramethylsilane as an internal standard. The resulting free induction decay (FID) signals were processed using MestRe-C software (version 4.9.9.6). Chemical shifts (δ) in ^{1}H spectra are reported in ppm and referenced to the residual proton signal of deuterated chloroform, while for ^{13}C spectra, the chemical shifts correspond to the carbon signal of the deuterated solvent.

2.3. H_2 and CO_2 adsorption isotherms

H_2 adsorption isotherms (99.999%) at 77 K and 87 K were measured using a Hiden Analytical Intelligent Gravimetric Analyzer (IGA-003), which incorporates an ultra-high vacuum system. Buoyancy effects were corrected by recording He (99.9999%) adsorption isotherms at 273 K prior to H_2 measurements. For high-pressure adsorption–desorption studies at room temperature (RT), a Quantachrome iSorbHP1 volumetric analyzer was employed, operating within a pressure range of 0.06–200 bar. The Helmholtz real-gas equation of state (EOS) was applied to calculate H_2 density values based on National Institute of Standards and Technology (NIST) reference data.[43] The Virial 2 equation was utilized to model the adsorption isotherms and fit the experimental data.

Pure CO_2 adsorption isotherms were obtained using a Micromeritics 3Flex Adsorption Analyzer. Prior to measurement, approximately 100 mg of MOF sample was subjected to *in situ* evacuation under vacuum (9 × 10^{-6} bar) at 120 °C for 12 h, ensuring complete removal of adsorbed species. After degassing, the sample was cooled to the desired analysis temperature using a thermostatic polyethylene glycol bath. Experimental CO_2 adsorption isotherms at 273 K and 298 K were fitted using the Sips equation.

The enthalpy of adsorption for H_2 and CO_2 was determined by applying the Clausius–Clapeyron equation.[44] For H_2 adsorption, data recorded at 273 K, 298 K, and 323 K (up to 170 bar) were utilized, while for CO_2, isotherm data collected at 273 K and 298 K (up to 1 bar) were used. The adsorption enthalpy was calculated from the slope of the best linear fit of ln(P) *versus* ($1/T$) at each CO_2 loading.

2.4. Catalytic cycloaddition reaction of CO_2

In a typical catalytic test, 1 mmol of epoxide was combined with a degassed MOF catalyst (1.5 mol%, calculated as the ratio of active metal sites to epoxide) and 0.05 mmol of tetrabutylammonium bromide (TBAB) in a 100 mL stainless-steel autoclave[45] (Scheme 1). Prior to pressurization, the system

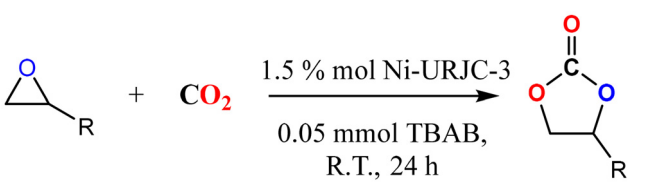

Scheme 1 Cycloaddition reaction of epoxides with 12 bar of CO_2 catalyzed by Ni-URJC-3 and TBAB.

underwent three evacuation cycles with CO_2 to remove residual gases. The reaction proceeded at ambient temperature under continuous moderate stirring for 24 h. After completion, the remaining CO_2 was released gradually to avoid abrupt depressurization. The MOF catalyst was recovered by centrifugation for potential reuse.

To evaluate reaction conversion and selectivity, the resulting products were analyzed by ^{1}H NMR spectroscopy, employing $CDCl_3$ as the solvent and 1,2,4,5-tetrachloro-3-nitrobenzene as an internal standard.

3. Results and discussion

3.1. Structural characterization of the Ni-URJC-3

Crystals of Ni-URJC-3 were obtained after 72 hours of reaction under acidic solvothermal conditions in DMF. The crystal structure comprises pairs of Ni(II) atoms bridged by two carboxylate groups from two adjacent $ABTC^{-4}$ ligands. One of the Ni(II) centers is further coordinated to two chelating carboxylate groups from two $ABTC^{-4}$ ligands forming a distorted octahedral coordination geometry. The second Ni(II) centre is further coordinated to three DMF molecules and an oxygen from a chelating carboxylate group forming an octahedral coordination geometry. The Ni–O bond distances were in the 1.988(8)–2.172(9) Å, typical of Ni(II)–carboxylate and Ni(II)–DMF bonds. The resulting Ni_2O_{11} secondary building unit expands forming a tetrahedral node (Fig. 1a) interconnected by $ABTC^{-4}$ ligands forming a 3D network with channels through the (110) and (001) directions (Fig. 1b and c), filled by 2.5 DMF molecules per formula unit. For a more detailed view of the crystal structure, including atom labelling and coordination geometry, please refer to Fig. S2, Tables S1 and S2.

Fig. 2 shows the comparison of the diffraction pattern of Ni-URJC-3 obtained by the X-ray diffraction technique with the simulated pattern obtained from the single crystal of the MOF structure, which allows for corroborating both the correct elucidation of the MOF structure and the presence of the unique desired phase.

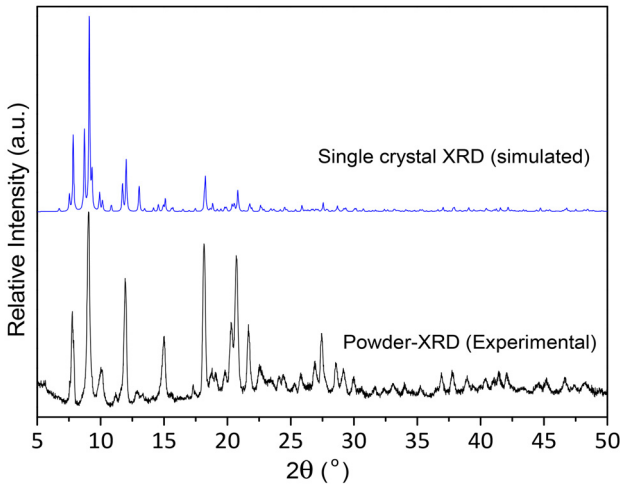

Fig. 2 The simulated and experimental patterns of Ni-URJC-3 material.

Once the crystalline structure of the material was confirmed, the physicochemical characterization was completed. First, it can be observed by SEM images (Fig. 3) that the synthesized sample is constituted only by large crystals (≈50 μm), being cubic in shape. The crystals can be observed in agglomerates or in isolation, exhibiting the same morphological characteristics.

The thermogravimetric analysis carried out to check the thermal stability of the new material shows three weight losses (Fig. 4). The first of minor proportion, occurs up to about 70 °C, and is due to the evaporation of the water molecules retained on the surface of the crystals due to the humidity of the environment. The second weight loss, which starts at 120 °C and is centered at 210 °C, may correspond to the elimination of DMF molecules inside the cavities and those strongly coordinated. This loss is followed by decomposition of the framework because of the organic ligand calcination in the range of 350–400 °C and the consequent collapse of the crystalline structure.

Based on these results, it was evident that coordinated DMF molecules remain within the framework after synthesis.

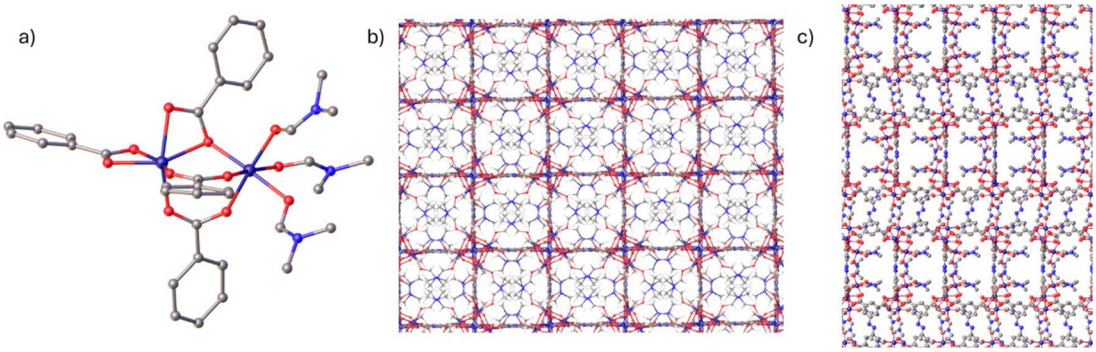

Fig. 1 Crystal structure of Ni-URJC-3 showing (a) the tetrahedral nodes of the secondary building unit; and the pores occupied by coordinated DMF in the (b) (001) direction and (c) (110) direction. Colour code: Ni in dark blue, nitrogen in light blue, oxygens in red and carbons in grey. Hydrogen and solvated DMF were removed for clarity.

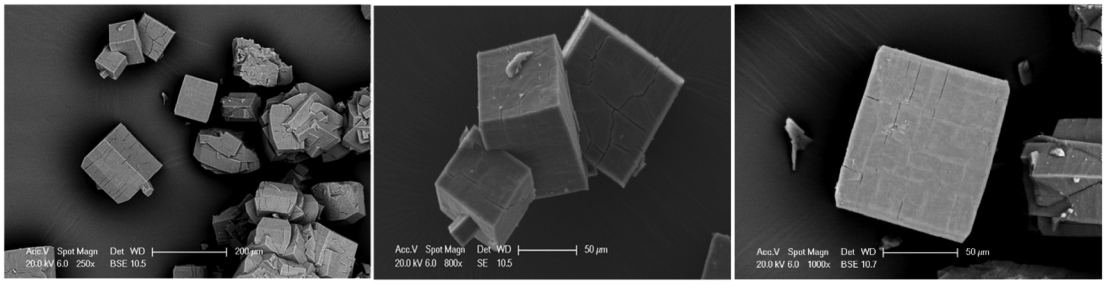

Fig. 3 SEM images of Ni-URJC-3.

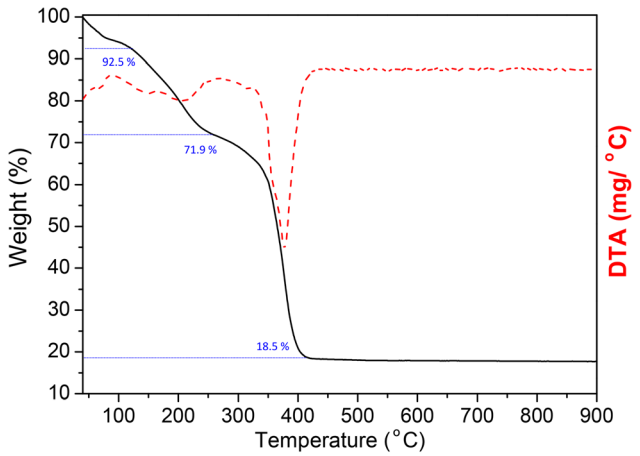

Fig. 4 TG/DTG analyses of Ni-URJC-3.

In an effort to remove them and achieve proper activation of the material, several solvent-exchange experiments were carried out using acetone, methanol, acetonitrile and dichloromethane as lower-boiling solvents. However, powder X-ray diffraction analyses of the exchanged samples (Fig. S4) revealed a marked loss of crystallinity and partial structural degradation, indicating that Ni-URJC-3 is not stable in these media. Likewise, according to the TGA results, the removal of coordinated DMF would require activation temperatures close to 200 °C. Nevertheless, when the sample was degassed at 180 °C under vacuum, a complete collapse of the framework was observed by powder X-ray diffraction (Fig. S5). Therefore, activation was ultimately performed at 120 °C under high vacuum for 12 h, as a compromise condition that preserves the crystalline structure (Fig. S6) while inevitably retaining a fraction of coordinated DMF within the pores.

Fig. 5 shows Ni-URJC-3 isotherm that could be classified between type I and type II according to the IUPAC classification.[46] At low P/P_0 values, the typical sharp increase of microporous materials was evidenced, while at higher pressures the increase of Ar adsorbed is progressive, not reaching the plateau, which is characteristic of macropores filling. This may be due to interparticle adsorption. This material presents a S_{BET} of 158 $m^2\ g^{-1}$ and a pore volume of 0.074 $cm^3\ g^{-1}$. These results indicate a discrepancy between the observed porosity and the crystal structure determined by single crystal X-ray diffraction, where the pores occupy 41% of the volume of the unit cell. The pore size distribution (PSD) of the new material has also been plotted, showing a bimodal distribution with the first maximum centered at 5.6 Å, and the second around 12 Å. This allows the Ar to partially enter into the cavities of the material, since the kinetic diameter of the argon molecule (3.5 Å) is similar to the smallest cavity size, so the gas cannot easily diffuse through those pores. It is noteworthy

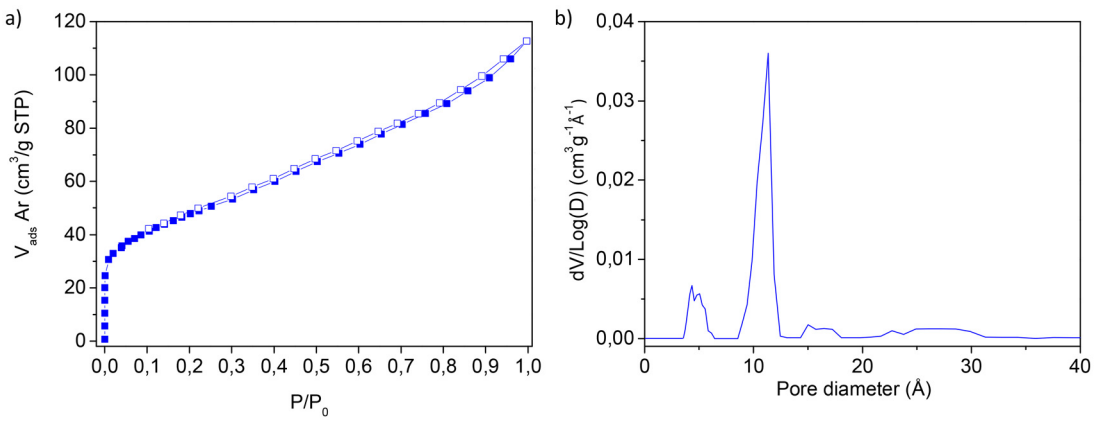

Fig. 5 Argon adsorption/desorption isotherm at 87 K (a) and PSD (b) of the Ni-URJC-3 material.

that the coordinated DMF molecules bound to the nickel centers could not be completely removed, which limits the accessibility of the porous system and contributes to the lower experimental surface area compared to the theoretical one.

3.2. Hydrogen adsorption isotherms

The material has been subjected to a series of hydrogen adsorption tests by varying pressure and temperature conditions. Prior to that, the material activation process was undertaken under conditions similar to those employed in the argon analysis isotherm, namely at 120 °C and high vacuum for a period of 12 hours. Fig. 6 shows the hydrogen adsorption isotherms, on a volumetric and gravimetric basis, at cryogenic temperature (77 K).

At 77 K and 16 bar, Ni-URJC-3 reaches a gravimetric hydrogen adsorption capacity of 3.7 wt%. Considering the direct correlation between hydrogen uptake and the specific surface area (S_{BET}) at cryogenic temperatures, this value is remarkably high. It surpasses the capacities reported for other MOF materials such as ZIF-8 (V_p = 0.64 cm^3 g^{-1}; S_{BET} = 1630 m^3 g^{-1}), MIL-100(Fe) (V_p = 0.83 cm^3 g^{-1}; S_{BET} = 2155 m^3 g^{-1}), and MOF-74(Mg) (V_p = 0.39 cm^3 g^{-1}; S_{BET} = 1510 m^2 g^{-1}), which exhibit hydrogen uptakes of 3.3, 2.5, and 3.01 wt%, respectively.[47–50] Furthermore, the performance of Ni-URJC-3 is also higher than that of other Ni-based MOFs or those incorporating organic ligands with azo groups in their structure, as shown in Table 1.

Due to the microporous nature of the Ni-URJC-3 material, the high adsorption values could be related to the presence of strong H_2-MOF interactions because of the confinement effect of hydrogen molecules within the smallest cavities of the structure, as well as its chemical nature, particularly the presence of Lewis acid and basic sites such as the nickel clusters and the azo groups, respectively, in the organic ligand. As the kinetic diameter of H_2 (2.89 Å) is smaller than that of Ar (3.40 Å), the hydrogen molecule could diffuse through the smaller cavities of the material. Table 2 summarizes the gravimetric and volumetric storage capacity of the novel material at the cited conditions. The small differences between the excess and total values are due to the small pore volume of the structure, so

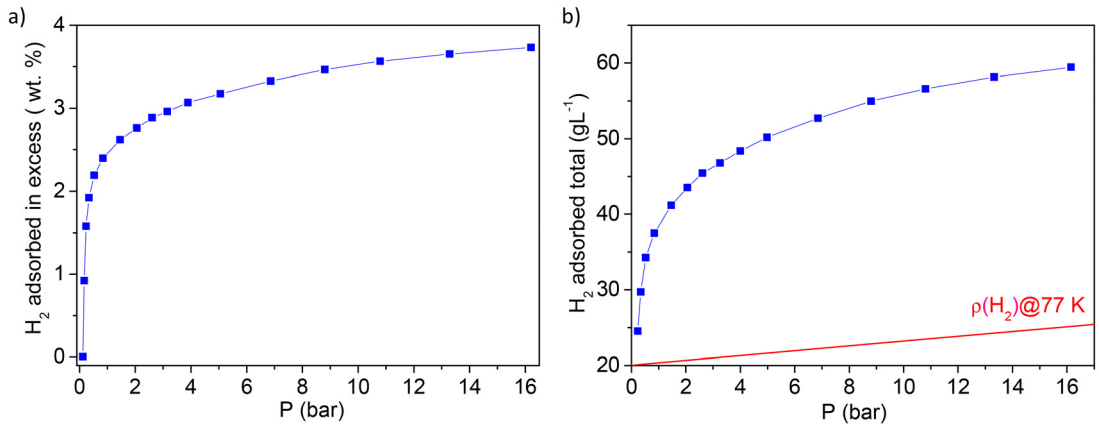

Fig. 6 Isotherms of excess hydrogen adsorption on gravimetric basis (a) and storage volume density (b).

Table 1 H_2 adsorption at 77 K of different Ni-based MOF and MOF with azo group in their structure

Material	S_{BET} (m^2 g^{-1})	Temperature (K)	P (bar)	H_2 Ad. (% wt)	Ref.
Ni-URJC-3	**158**	77	**1**	**2.39**	**This work**
			16	**3.7**	
$Ni_2(BDC)_2(dabco)$	1809	77	1	1.99	51
$Ni_2(BTEC)(bipy)_3$	766			1.28	
Ni(cyclam)(4,4′-bpydc)	—	77	1	1.1	52
Ni(HBTC)(4,4′-bipy)	1590	77	72	3.42	53
Ni(ox)(4,4′-bipy)	—	77	1	0.16	54
$Ni^{II}Ni^{III}$ (μ_3-OH)$(IN)_3(BDC)_{1.5}$	571	77	1	1.47	55
$Ni_3(OH)(pbpc)_3$	1553	77	1	1.99	56
$Ni_3O(TATB)_2$	—	77	1	0.63	57
$Ni_{2.75}Mn_{0.25}[(MnCl)_3(BTT)_8]$	554	77	1.2	2.29	58
Ni(dhtp)		77	1	2.1	59
JUC-62	2037	77	40	4.71	60
Zn-Azo	132	77	1	1.00	61
Co-URJC-3	171	77	1	2.25	62
			16	3.52	

Table 2 Hydrogen storage capacities of Ni-URJC-3 material, at 77 K and 16 bar

H_2 excess (wt%)	H_2 total (wt%)	H_2 excess (g L^{-1})	H_2 total (g L^{-1})	mol_{H_2} : mol_{Me}
3.7	3.7	59.3	59.5	8.04

almost all of the gas molecules are adsorbed on the surface of the material, instead of just filling the pores.

The Ni-URJC-3 material exhibits a high total volumetric storage density, reaching 59.5 g L^{-1} at 16 bars, which is higher than those observed for compressed hydrogen at the same conditions (~22 g L^{-1}). The elevated adsorption values can be attributed to the material's high density. Indeed, this behaviour has already been observed in MOFs materials with constrained pore size, which have been employed for the selective separation of small molecules.[63]

The storage capacity achieved at room temperature (298 K) and high pressure (170 bar) reached moderate values of about 0.25 wt% (Table 3 and Fig. 7). This value is comparable to those achieved by other MOFs with higher specific surface areas, such as MOF-5 (V_p = 1.18 cm^3 g^{-1}; S_{BET} = 2296 m^2 g^{-1}) and PCN-5 (V_p = 1.18 cm^3 g^{-1}; S_{BET} = 2095 m^2 g^{-1}), whose gravimetric hydrogen adsorption capacities are 0.25 and 0.19 wt%, respectively.[35] These results suggest that a reduced pore size in the materials leads to a higher confinement effect of H_2 molecules inside the pores, which promotes stronger H_2-MOF interactions.

To ascertain the interaction strength between H_2 and Ni-URJC-3, the hydrogen adsorption enthalpy was calculated using the Clausius–Clapeyron equation, with the experimental data at different temperatures (Fig. S7) fitted to a Virial function.[64] Fig. 8 depicts the adsorption enthalpy profile of the material, which exhibits a value for the adsorption enthalpy at low H_2 coverage of −9 kJ mol^{-1}. The adsorption enthalpy profile declines abruptly from the aforementioned value of −9 kJ mol^{-1} to around −6 kJ mol^{-1} for higher overlayer, indicating the presence of preferential hydrogen adsorption sites. Consequently, the interaction energy diminishes as these sites are fully occupied.

Table 3 Hydrogen storage capacities of Ni-URJC-3 material, at 298 K and 170 bar

H_2 excess (wt%)	H_2 total (wt%)	H_2 excess (g L^{-1})	H_2 total (g L^{-1})	mol_{H_2} : mol_{Me}
0.25	0.34	3.7	5.2	0.51

3.3. CO_2 adsorption isotherms

As demonstrated in Fig. 9, the CO_2 adsorption isotherms were conducted at temperatures of 0 and 25 °C. The material was activated under identical conditions to those employed in the other adsorption analyses, namely 120 °C and vacuum, for a duration of 12 hours. The CO_2 adsorption capacity was 2.51 and 1.77 mmol g^{-1} at 0 and 25 °C, respectively, as can be seen in Fig. 9.

The amount of CO_2 adsorbed at both temperatures is moderate since the kinetic diameter of CO_2 (3.9 Å) is similar to the

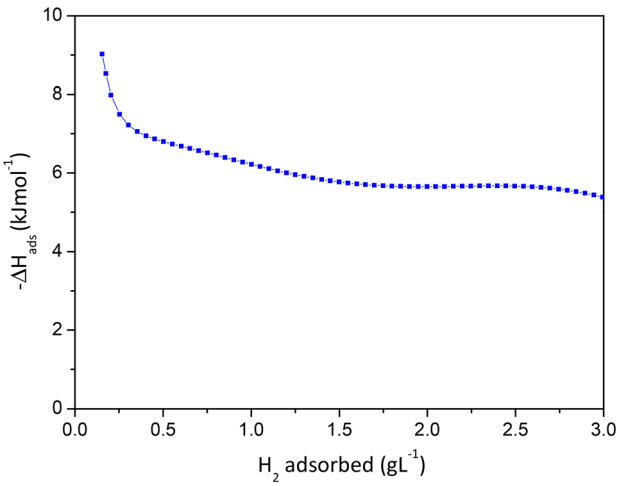

Fig. 8 Hydrogen adsorption enthalpy profile of Ni-URJC-3 material.

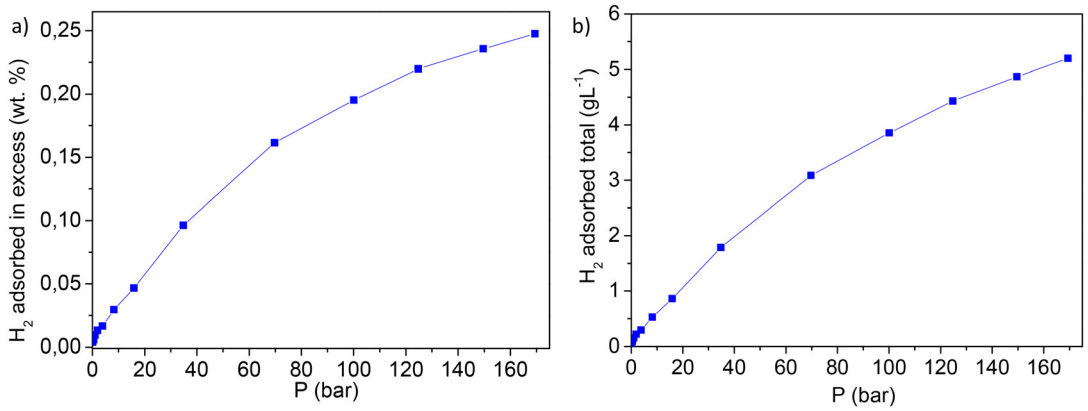

Fig. 7 Isotherms of excess hydrogen adsorption on gravimetric basis (a) and storage volume density (b) at 298 K of the Ni-URJC-3 material.

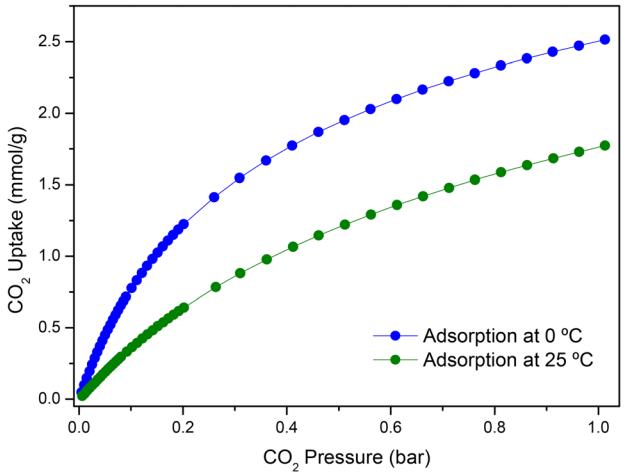

Fig. 9 CO_2 adsorption/desorption isotherms of Ni-URJC-3 at 0 and 25 °C.

smallest pores of the material, which led to a hindered diffusion of the gas through the cavities. The low-coverage CO_2 adsorption enthalpy of Ni-URJC-3 was found to be 25.9 kJ mol^{-1} (Fig. 10), which is higher or at least comparable to that of other Ni(II)-based MOF materials, including Ni-MOF (20.1 kJ mol^{-1})[65] and Ni-MOF-184 (36 kJ mol^{-1}),[66] which exhibit superior textural properties. The relatively high-CO_2 adsorption enthalpy of this material can be related to the presence of the azo group in the organic linker which acts as Lewis basic sites.[67]

3.4. Cycloaddition reaction

Table 4 summarizes the conversion, selectivity and turnover number (TON) values obtained in CO_2 cycloaddition reactions using five epoxides with different sizes, evaluated under reaction conditions of 1 mmol of epoxide, 12 bar of CO_2, 1.5 mol% (active metal sites/epoxide ratio) of degassed MOF catalyst, and 0.05 mmol of tetrabutylammonium bromide (TBAB) as cocatalyst for 24 hours. The TON was calculated as the ratio between the number of mol of product obtained and the number of mol of active metal sites in the catalyst. The number of active sites was estimated from the theoretical formula of the MOF, assuming that each unit cell of Ni-URJC-3 contains two nickel atoms acting as potential active sites.

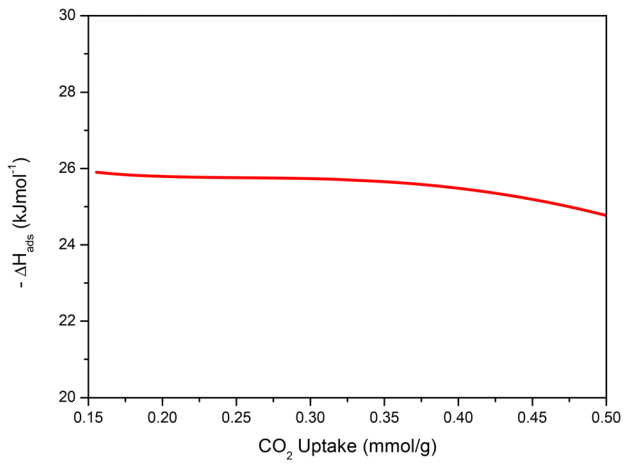

Fig. 10 CO_2 adsorption enthalpy profile of Ni-URJC-3 material.

Regarding, these results, the epoxide conversion values decrease markedly in the presence of epoxides with bulky groups. The conversion of epoxides containing smaller alkene chains is notably higher than that of the longer chain counterparts, indicating that the transport within the MOF porous system represents a rate-limiting step. The TON values follow the same trend as the conversions, decreasing markedly with the increase in the size and steric hindrance of the epoxide molecules.

The Ni-URJC-3 catalyst contains two principal channels of different dimensions. The larger channels are accessible to all epoxides, facilitating their entry and interaction, whereas the narrower channels restrict the access to bulkier epoxides. This trend is exemplified by propylene oxide and epichlorohydrin, which exhibits a conversion of 99 and 92%, respectively. However, when 1,2-epoxihexane, allyl glycidyl ether and styrene oxide were employed as substrates, the conversion decreased to 73, 71 and 34%, respectively. The increased steric hindrance occurring within the cavities was attributed to this phenomenon. This phenomenon has been previously reported in the literature for both organocatalysts and metal–organic frameworks.[68] The selectivity to cyclic carbonates was highly favorable for the smaller epoxides, exhibiting a selectivity over 99%. However, for styrene oxide, allyl glycidyl ether and 1,2-epoxyhexane, the selectivity is diminished due to the more favorable cyclodimerization reaction of the epoxide where CO_2 does not take part of the process (Scheme 2).[69] The selectivity in the case of styrene oxide was 68%, which was higher than that of 1,2-epoxyhexane, with a single chain, at 58%. The TON values exhibit the same trend observed for conversion, with higher values for propylene oxide and epichlorohydrin (33 and 31, respectively) and lower values for 1,2-epoxyhexane, allyl glycidyl ether and styrene oxide (14, 17 and 8, respectively). This correlation between TON, conversion and selectivity indicates that the catalytic efficiency of Ni-URJC-3 is strongly influenced by both steric constraints and the occurrence of side reactions that reduce the amount of desired cyclic carbonate formed.

In order to overcome the limitations observed at room temperature, cycloaddition reactions were carried out at 80 °C, maintaining all other reaction conditions similar to those indicated in Table 5. A notable increase in conversion values was observed for high-volume epoxides, including 1,2-epoxyhexane, allyl glycidyl ether and styrene oxide, with conversions exceeding of 99% for all substrates. This notable improvement underscores the versatility of the Ni-URJC-3 as catalyst, which enables better catalytic performance for sterically hindered substrates under mild temperature conditions. Nevertheless, the selectivity towards the intended products was not enhanced, as it is similar to the results at room temperature, with values of 60%, 69%, and 57% for 1,2-epoxyhexane, allyl

Table 4 Reaction results for cycloaddition reaction between CO_2 and different epoxides at room temperature for 24 h and 12 bar of CO_2

Epoxide	Product	Conversion[a] (%)	Selectivity[a] (%)	TON[b]
	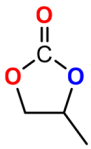	>99	>99	33
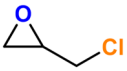	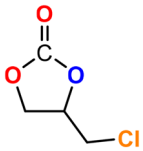	92	>99	31
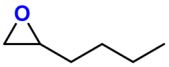	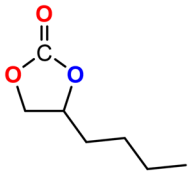	73	58	14
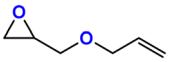	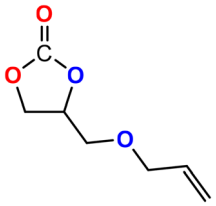	71	70	17
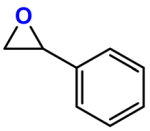	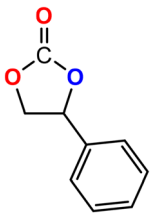	34	68	8

[a] Conversion and selectivity were determined by H-RMN. [b] TON = (mmol product)/(mmol Ni in catalyst).

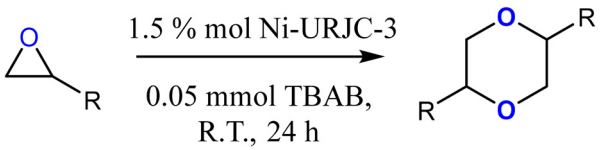

Scheme 2 Cyclodimerization reaction of epoxides catalyzed by Ni-URJC-3 and TBAB.

glycidyl ether, and styrene oxide, respectively. These findings demonstrate the ability of Ni-URJC-3 to achieve high conversions even for substrates with high steric issues, while maintaining a consistent selectivity profile. This behavior is clearly observed when comparing the TON values obtained at 80 °C with those achieved at room temperature, a clear increase is observed for all substrates, in agreement with the higher conversion levels reached under thermal activation. Values of 20, 23 and 19 were obtained for 1,2-epoxyhexane, allyl glycidyl ether and styrene oxide, respectively, while at room temperature the corresponding values were 14, 17 and 8. This improvement confirms that the increase in temperature enhances the catalytic efficiency of Ni-URJC-3, mainly as a result of overcoming diffusion limitations. Nevertheless, side reactions still restrict the selectivity towards the desired cyclic carbonates.

The catalytic activity of this material has been compared with other MOF materials reported in the literature, not only those based on Ni, but also on other metals such as Co or Zn, which typically exhibit higher catalytic activity due to their stronger Lewis acidity.[70] As shown in Table 6, Ni-URJC-3 displays a higher conversion of propylene oxide and epichlorohydrin than other MOFs reported in the literature, even under milder reaction conditions, such as a temperature of 25 °C.

Among the nickel-based catalysts, the catalytic performance exhibited by Ni-URJC-3 displays higher values than other nickel-based MOFs with larger textural properties, such as the Ni-MOF-74 material, which has a specific surface area of 1121 $m^2\ g^{-1}$ and a pore volume of 0.49 $cm^3\ g^{-1}$.[71] The better catalytic properties may be attributed, at least in part, to the presence of nitrogen heteroatoms in the organic ligand of Ni-URJC-3, whose basicity may play a pivotal role.[69] Prior works

Table 5 Reaction results for cycloaddition reaction between CO_2 and different epoxides at 80 °C for 24 h and 12 bar of CO_2

Epoxide	Product	Conversion[a] (%)	Selectivity[a] (%)	TON[b]
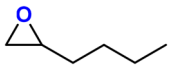	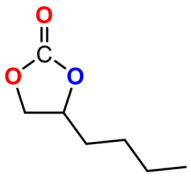	>99	60	20
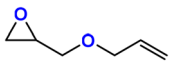	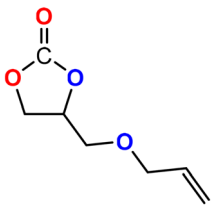	>99	69	23
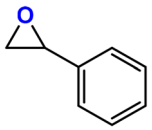	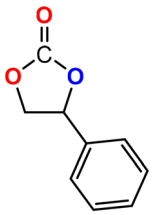	>99	57	19

[a] Conversion and selectivity were determined by H-RMN. [b] TON = (mmol product)/(mmol Ni in catalyst).

Table 6 Conversion of propylene oxide and epichlorohydrin of different MOF materials

Material	Pressure (bar)	Temp (°C)	Time (h)	Co-catalyst	Epoxide[a]	Conv. (%)	Ref.
Ni-URJC-3	**12**	**25**	**24**	**TBAB**	**PO**	**>99**	**This work**
					EPH	**92**	
Ni 2	1	40	40	TBAB	PO	98.4	74
Ni 3						99	
Ni-MOF-74	12	25	24	TBAB	EPH	79	70
Mn-URJC-13	12	25	24	TBAB	PO	99	75
					EPH	87	
Cu-URJC-1	12	25	24	TBAB	EPH	84	76
JUC-62	12	25	24	TBAB	EPH	83	
ZIF-8	12	25	24	TBAB	EPH	76	77
Co-AOIA	1	25	48	—	PO	57	78
Co-ANIA	1	25	48	—	PO	50	
Eu-MOF	20	80	24	TBAB	PO	38	79
Cu-MOF	1	90	24	TBAB	PO	99	80
Cu-BTC@$ZnFe_2O_4$	1	80	12	TBAB	PO	90	81
					EPH	76	
JLU-Liu-21	1	25	48	TBAB	PO	96	82
NUC-5	1	80	24	TBAB	PO	97	83
Mn-MOF-2	1	25	24	TBAB + 30 × 3 W	PO	100	84

[a] PO: propylene oxide. EPH: epichlorohydrin.

have established a correlation between the reactivity of CO_2 in cycloaddition reaction and the basicity of the functional groups present in MOF structures.[71–73]

To assess the potential for reuse of this MOF material catalyst in the cycloaddition reaction between CO_2 and epichlorohydrin, five consecutive catalytic cycles were performed using Ni-URJC-3, under identical reaction conditions previously established. The results demonstrate that this new MOF material exhibited a stable catalytic activity throughout at least five reaction cycles, achieving a 91% conversion of epichlorohydrin (Fig. 11a). Furthermore, the XRD pattern of the Ni-URJC-3 material after all reaction cycles (Fig. 11b) exhibits an identical profile, with the main diffraction peaks as in the synthesized material, specifically at 7.90, 9.15, 10.3, 12.15, and 15°. It can be concluded that this nickel-based MOF material is stable and, in turn, reusable in the cycloaddition reaction between carbon dioxide and epoxides, thereby widening the range of potential applications.

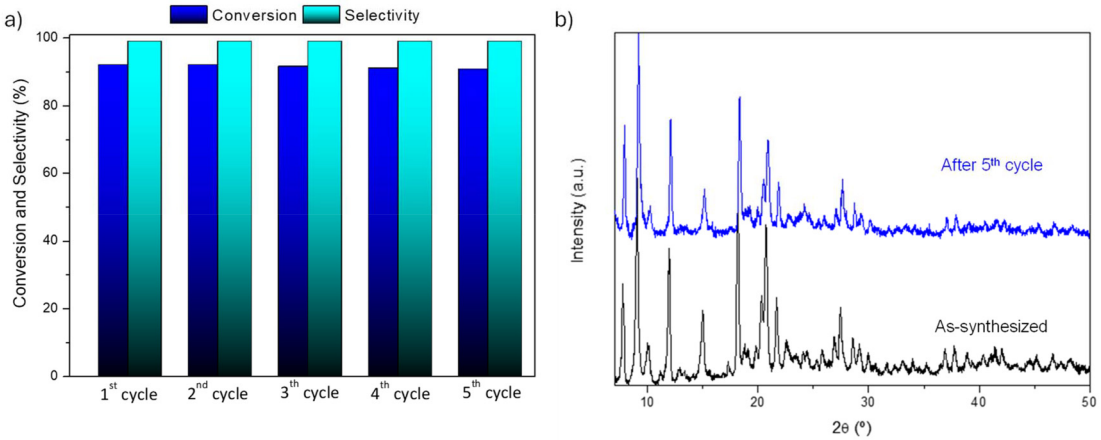

Fig. 11 Recyclability study (a), and the XRD pattern of Ni-URJC-3 (b) following the cycloaddition reaction between CO_2 and epichlorohydrin.

3.5. Catalytic cycle

Based on previously reported reaction mechanisms involving MOF materials that incorporate nitrogen-containing organic ligands with Lewis's base character,[85,86] we have proposed the following reaction mechanism illustrated in Fig. 12. The proposed reaction mechanism consists of four sequential steps, involving interactions between the metal ion, epoxides, the organic linker and CO_2. In the initial stage, the epoxide molecule coordinates with the nickel metal center *via* its oxygen atom, leading to molecular polarization. The bromide ion from TBAB then performs a nucleophilic attack on the less substituted carbon of the epoxide, inducing ring-opening and generating a reactive intermediate (Step II). In the third step, CO_2 interacts with the nitrogen atom of the organic ligand, enhancing its nucleophilic nature. This increase in nucleophilicity facilitates a

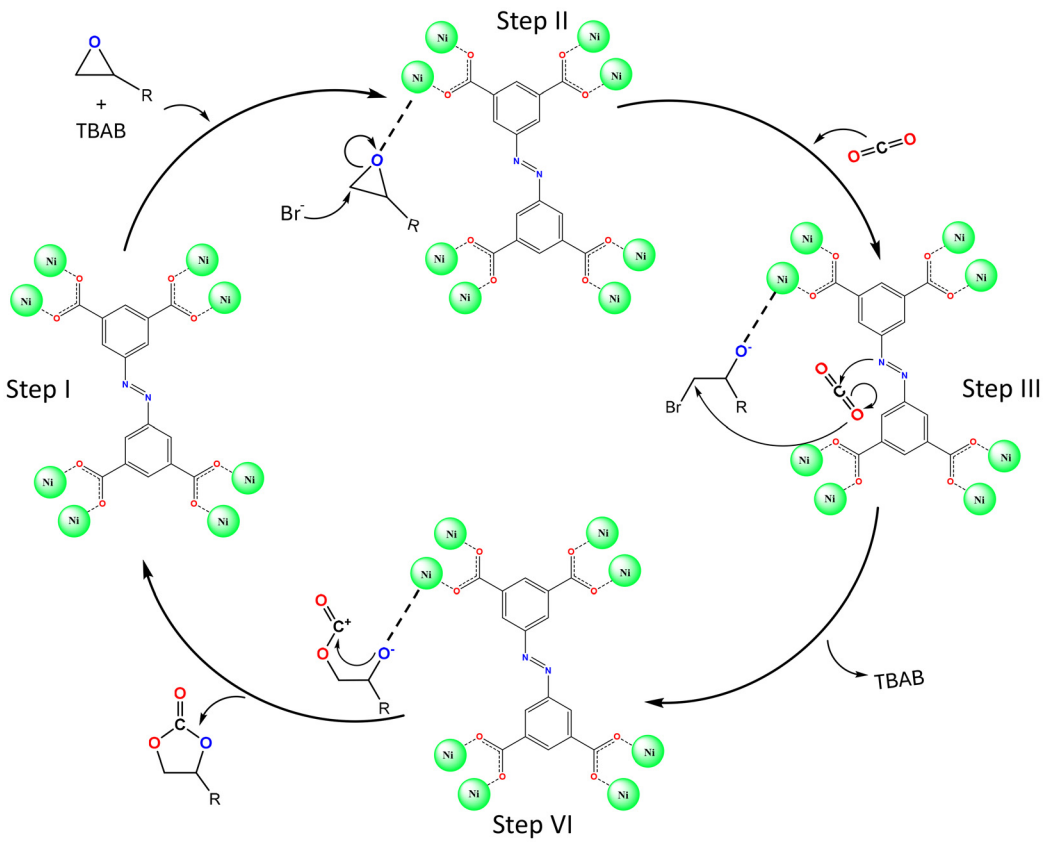

Fig. 12 Catalytic cycle of cycloaddition reaction between CO_2 and epoxides catalyzed by Ni-URJC-3.

nucleophilic attack by an oxygen atom of CO_2 on the carbon bonded to the bromide ion, ultimately displacing the bromide. Finally, in the step IV, the intermediate formed in Step III undergoes an intramolecular nucleophilic attack, where the oxygen from the epoxide attacks the carbon of CO_2, leading to ring closure and the formation of the cyclic carbonate.

4. Conclusions

A novel material, designated Ni-URJC-3, has been successfully synthesized through the coordination of the organic ligand 5,5′-(diazene-1,2-diyl)diisophthalic acid (H_4ABTC). The crystal structure is formed by pairs of Ni(II) atoms bridged and chelated by carboxylates from four adjacent ABTC-4 ligands, resulting in the formation of a tetrahedral secondary building unit (SBU). These SBUs are further interconnected by ABTC-4 ligands to form a three-dimensional porous network. The Ni-URJC-3 material contains structural Lewis acid and basic groups given by the nickel and the azo groups, respectively. Moreover, it displays a bimodal pore size distribution, with a peak centered at 5 and 12 Å. Despite its relatively small specific surface area, the material exhibits a notable hydrogen adsorption capacity (3.7 wt% and 59.5 g L^{-1}, at 77 K and 16 bar), attributed to the presence of the Lewis sites and confinement effect of the hydrogen molecules within the microcavities, improving the interaction between the hydrogen molecules and the MOF structure. The hydrogen adsorption enthalpy is −9 kJ mol^{-1}, comparable to other microporous MOF materials exhibiting exposed metal sites or moderate-to-high interaction with H_2 molecules, reported in the literature. In the case of CO_2, the adsorption capacity is somehow constrained by the fact that the kinetic diameter of the gas molecule is similar to the smaller cavities of the Ni-URJC-3 material. Nevertheless, the adsorption enthalpy of CO_2 is higher than that of other nickel MOF materials with superior textural properties. Furthermore, Ni-URJC-3 has been identified as a promising heterogeneous catalyst for epoxide cycloaddition reactions in the context of CO_2 valorization. The catalytic performance of the Ni-URJC-3 material surpasses to that of other nickel-based MOF materials with much larger specific surface areas, irrespective of the size of the epoxide employed. This is due to the presence of the azo group (N=N) in the organic ligand of the material, which acts as a Lewis base, thereby facilitating reactivity with CO_2 Furthermore, the material is reusable as a heterogeneous catalyst in CO_2 transformation, exhibiting both structural and catalytic stability after five consecutive cycles. In view of the aforementioned characteristics, the novel Ni-URJC-3 is a multifunctional material with potential application in various environmental contexts, such as gas adsorption and CO_2 valorization.

Author contributions

Elena García Rojas: Investigation, formal analysis, writing – original draft. Helena Montes-Andrés: Conceptualization, methodology, investigation. Jesús Tapiador: Methodology, investigation, formal analysis, writing – original draft. Carmen Martos: Supervision, resources, project administration, funding acquisition. Pablo Salcedo-Abraira: Investigation, formal analysis, writing – original draft. Duane Choquesillo-Lazarte: Investigation, formal analysis. Gisela Orcajo: Writing – review & editing, supervision, resources, project administration, funding acquisition. Pedro Leo: Conceptualization, methodology, formal analysis, writing-original draft, writing – review & editing.

Conflicts of interest

There are no conflicts to declare.

Data availability

The data supporting this article have been included as part of the manuscript. The research data is available in the Universidad Rey Juan Carlos repository.

Supplementary information (SI): synthesis of 5,5′-(diazene-1,2-diyl)diisophthalic acid ligand [H_4ABTC], crystal data and structure refinement for Ni-URJC-3. XRD of the material after solvent-exchange stability tests, adsorption isotherm of H_2 at temperatures 273, 298 and 323 K and ^{1}H NMR of reactions. See DOI: https://doi.org/10.1039/d5dt02218e.

CCDC 2391335 contains the supplementary crystallographic data for this paper.[87]

Acknowledgements

The authors gratefully acknowledge the financial support of Spanish Ministry of Science and Innovation to the ECOCAT Project (PID2022-136321OA-C22) and Universidad Rey Juan Carlos for IMPULSO Project (Grant M-3729). P.S.-A. thanks Juan de la Cierva Grant JDC2022-048964-I funded by MICIU/AEI/10.13039/501100011033 and by "European Union NextGenerationEU/PRTR".

References

1 International Energy Agency.
2 A. Schoedel, Z. Ji and O. M. Yaghi, *Nat. Energy*, 2016, **1**, 1–13.
3 Y. Ma, Z. Wang, X. Xu and J. Wang, *Chin. J. Catal.*, 2017, **38**, 1956–1969.
4 J. M. Harris and B. Roach, Global Climate Change: Science and Economics, in *Environmental and Natural Resource Economics: A Contemporary Approach*, 2021, ch. 12, pp. 1–33.
5 F. Wang, J. D. Harindintwali, Z. Yuan, M. Wang, F. Wang, S. Li, Z. Yin, L. Huang, Y. Fu, L. Li, S. X. Chang, L. Zhang, J. Rinklebe, Z. Yuan, Q. Zhu, L. Xiang, D. C. W. Tsang, L. Xu, X. Jiang, J. Liu, N. Wei, M. Kästner, Y. Zou, Y. S. Ok,

J. Shen, D. Peng, W. Zhang, D. Barceló, Y. Zhou, Z. Bai, B. Li, B. Zhang, K. Wei, H. Cao, Z. Tan, L. bin Zhao, X. He, J. Zheng, N. Bolan, X. Liu, C. Huang, S. Dietmann, M. Luo, N. Sun, J. Gong, Y. Gong, F. Brahushi, T. Zhang, C. Xiao, X. Li, W. Chen, N. Jiao, J. Lehmann, Y. G. Zhu, H. Jin, A. Schäffer, J. M. Tiedje and J. M. Chen, *Innovation*, 2021, **2**, 100180.

6 L. Jensen, Sustainable carbon cycles, European Commission, 2022, pp. 1–8.

7 A. H. Farmahini, S. Krishnamurthy, D. Friedrich, S. Brandani and L. Sarkisov, *Chem. Rev.*, 2021, **121**, 10666–10741.

8 S. Bao, X. Zheng, Z. Xu, B. Ji, Z. Yang, W. Sun, L. Guo, Y. Zhu, J. Mei, J. Rong and Z. Li, *J. Environ. Chem. Eng.*, 2025, **13**, 115171.

9 X. Zhao, S. Yang, S. Ebrahimiasl, S. Arshadi and A. Hosseinian, *J. CO_2 Util.*, 2019, **33**, 37–45.

10 M. Kou, W. Liu, Y. Wang, J. Huang, Y. Chen, Y. Zhou, Y. Chen, M. Ma, K. Lei, H. Xie, P. K. Wong and L. Ye, *Appl. Catal., B*, 2021, **291**, 120146.

11 K. T. Liu, J. Y. Chuang, R. J. Jeng and M. K. Leung, *ACS Omega*, 2021, **6**, 27279–27287.

12 E. J. C. Lopes, A. P. C. Ribeiro and L. M. D. R. S. Martins, *Catalysts*, 2020, **10**, 479.

13 P. J. Megia, A. J. Vizcaino, J. A. Calles and A. Carrero, *Energy Fuels*, 2021, **35**, 16403–16415.

14 B. C. Tashie-Lewis and S. G. Nnabuife, *Chem. Eng. J. Adv.*, 2021, **8**, 100172.

15 IEA, Global Hydrogen Review 2021, OECD Publishing, Paris, 2021.

16 M. Amin, H. H. Shah, A. G. Fareed, W. U. Khan, E. Chung, A. Zia, Z. U. R. Farooqi and C. Lee, *Int. J. Hydrogen Energy*, 2022, **47**, 33112–33134.

17 A. M. Oliveira, R. R. Beswick and Y. Yan, *Curr. Opin. Chem. Eng.*, 2021, **33**, 100701.

18 R. R. Ratnakar, N. Gupta, K. Zhang, C. van Doorne, J. Fesmire, B. Dindoruk and V. Balakotaiah, *Int. J. Hydrogen Energy*, 2021, **46**, 24149–24168.

19 M. Soleymani, V. Mostafavi, M. Hebert, S. Kelouwani and L. Boulon, *Int. J. Hydrogen Energy*, 2024, **91**, 137–171.

20 A. I. Osman, M. Nasr, A. S. Eltaweil, M. Hosny, M. Farghali, A. S. Al-Fatesh, D. W. Rooney and E. M. Abd El-Monaem, *Int. J. Hydrogen Energy*, 2024, **67**, 1270–1294.

21 K. P. Brooks, S. J. Sprik, D. A. Tamburello and M. J. Thornton, *Int. J. Hydrogen Energy*, 2018, **43**, 8846–8858.

22 U.S. Department of Energy, DOE Technical Targets for Onboard Hydrogen Storage for Light-Duty Vehicles, https://www.energy.gov/eere/fuelcells/doe-technical-targets-onboard-hydrogen-storage-light-duty-vehicles.

23 C. Grady, S. McWhorter, M. Sulic, S. J. Sprik, M. J. Thornton, K. P. Brooks and D. A. Tamburello, *Int. J. Hydrogen Energy*, 2022, **47**, 29847–29857.

24 F. Alasali, M. I. Abuashour, W. Hammad, D. Almomani, A. M. Obeidat and W. Holderbaum, *Energy Sci. Eng.*, 2024, **12**, 1934–1968.

25 A. Laalam and P. Bazazi, *Int. J. Hydrogen Energy*, 2025, **169**, 151057.

26 S. E. M. Elhenawy, M. Khraisheh, F. Almomani and G. Walker, *Catalysts*, 2020, **10**, 1–33.

27 A. Islam, A. Malek, S. H. Teo, H. M. Marwani, M. M. Rahman, A. M. Asiri, M. A. R. Khan, Y. H. Taufiq-Yap and Md. R. Awual, *Sustainable Mater. Technol.*, 2023, **37**, e00636.

28 Z. A. Sandhu, M. A. Raza, N. S. Awwad, H. A. Ibrahium, U. Farwa, S. Ashraf, A. Dildar, E. Fatima, S. Ashraf and F. Ali, *Mater. Adv.*, 2024, **5**, 30–50.

29 R. Jasrotia, Himanshi, B. Lal, Suman, M. Ramya, G. Katoch, S. Singh and C. C. Kit, *Results Eng.*, 2025, **27**, 106844.

30 R. Shah, S. Ali, F. Raziq, S. Ali, P. M. Ismail, S. Shah, R. Iqbal, X. Wu, W. He, X. Zu, A. Zada, Adnan, F. Mabood, A. Vinu, S. H. Jhung, J. Yi and L. Qiao, *Coord. Chem. Rev.*, 2023, **477**, 214968.

31 J. Pang, Z. Zhang, S. Zhang, X. Guo, Q. Chen, X.-W. Zhang, H.-L. Zhou, W. Gong, S. S. A. Shah, C. Zhong, J.-R. Li, J.-P. Zhang, Y. Cui, H.-L. Jiang and X.-H. Bu, *Sci. China: Chem.*, 2025, **68**, 1230–1286.

32 W. Lu, Z. Wei, Z. Y. Gu, T. F. Liu, J. Park, J. Park, J. Tian, M. Zhang, Q. Zhang, T. Gentle, M. Bosch and H. C. Zhou, *Chem. Soc. Rev.*, 2014, **43**, 5561–5593.

33 Y. Zhang, Y. Zhang, X. Wang, J. Yu and B. Ding, *ACS Appl. Mater. Interfaces*, 2018, **10**, 34802–34810.

34 R. Mogale, J. Conradie and E. H. G. Langner, *Molecules*, 2022, **27**, 1370.

35 M. P. Suh, H. J. Park, T. K. Prasad and D. W. Lim, *Chem. Rev.*, 2012, **112**, 782–835.

36 S. P. Shet, S. Shanmuga Priya, K. Sudhakar and M. Tahir, *Int. J. Hydrogen Energy*, 2021, **46**, 11782–11803.

37 A. Dhakshinamoorthy, M. Alvaro, H. Chevreau, P. Horcajada, T. Devic, C. Serre and H. Garcia, *Catal. Sci. Technol.*, 2012, **2**, 324–330.

38 Bruker, *APEX III*, Bruker AXS Inc., Madison, Wisconsin, USA, 2019.

39 G. M. Sheldrick, *Acta Crystallogr., Sect. A: Found. Adv.*, 2015, **71**, 3–8.

40 O. V. Dolomanov, L. J. Bourhis, R. J. Gildea, J. A. K. Howard and H. Puschmann, *J. Appl. Crystallogr.*, 2009, **42**, 339–341.

41 S. Brunauer, P. H. Emmett and E. Teller, *J. Am. Chem. Soc.*, 2002, **60**, 309–319.

42 J. Jagiello and M. Thommes, *Carbon*, 2004, **42**, 1227–1232.

43 J. W. Leachman, R. T. Jacobsen, S. G. Penoncello and E. W. Lemmon, *J. Phys. Chem. Ref. Data*, 2009, **38**, 721–748.

44 A. L. Myers, *AIChE J.*, 2002, **48**, 145–160.

45 J. Tapiador, E. García-Rojas, P. López-Patón, G. Calleja, G. Orcajo, C. Martos and P. Leo, *J. Environ. Chem. Eng.*, 2023, **11**, 109497.

46 M. Thommes, K. Kaneko, A. V. Neimark, J. P. Olivier, F. Rodriguez-Reinoso, J. Rouquerol and K. S. W. Sing, *Pure Appl. Chem.*, 2015, **87**, 1051–1069.

47 K. S. Park, Z. Ni, A. P. Côté, J. Y. Choi, R. Huang, F. J. Uribe-Romo, H. K. Chae, M. O'Keeffe and O. M. Yaghi, *Proc. Natl. Acad. Sci. U. S. A.*, 2006, **103**, 10186–10191.

48 M. Latroche, S. Surblé, C. Serre, C. Mellot-Draznieks, P. L. Llewellyn, J. H. Lee, J. S. Chang, H. J. Sung and G. Férey, *Angew. Chem., Int. Ed.*, 2006, **45**, 8227–8231.
49 K. Sumida, C. M. Brown, Z. R. Herm, S. Chavan, S. Bordiga and J. R. Long, *Chem. Commun.*, 2011, **47**, 1157–1159.
50 J. L. C. Rowsell, A. R. Millward, K. S. Park and O. M. Yaghi, *J. Am. Chem. Soc.*, 2004, **126**, 5666–5667.
51 P. Song, Y. Li, B. He, J. Yang, J. Zheng and X. Li, *Microporous Mesoporous Mater.*, 2011, **142**, 208–213.
52 E. Y. Lee and M. P. Suh, *Angew. Chem., Int. Ed.*, 2004, **43**, 2798–2801.
53 Y. Li, L. Xie, Y. Liu, R. Yang and X. Li, *Inorg. Chem.*, 2008, **47**, 10372–10377.
54 J. Lee, J. Li and J. Jagiello, *J. Solid State Chem.*, 2005, **178**, 2527–2532.
55 G. Jiang, T. Wu, S.-T. Zheng, X. Zhao, Q. Lin, X. Bu and P. Feng, *Cryst. Growth Des.*, 2011, **11**, 3713–3716.
56 J. Jia, X. Lin, C. Wilson, A. J. Blake, N. R. Champness, P. Hubberstey, G. Walker, E. J. Cussen and M. Schröder, *Chem. Commun.*, 2007, 840–842.
57 S. Ma, X.-S. Wang, E. S. Manis, C. D. Collier and H.-C. Zhou, *Inorg. Chem.*, 2007, **46**, 3432–3434.
58 M. Dincă and J. R. Long, *J. Am. Chem. Soc.*, 2007, **129**, 11172–11176.
59 W. Zhou, H. Wu and T. Yildirim, *J. Am. Chem. Soc.*, 2008, **130**, 15268–15269.
60 M. Xue, G. Zhu, Y. Li, X. Zhao, Z. Jin, E. Kang and S. Qiu, *Cryst. Growth Des.*, 2008, **8**, 2478–2483.
61 L.-W. Lee, T.-T. Luo, S.-H. Lo, G.-H. Lee, S.-M. Peng, Y.-H. Liu, S.-L. Lee and K.-L. Lu, *CrystEngComm*, 2015, **17**, 6320–6327.
62 H. Montes-Andrés, P. Leo, G. Orcajo, A. Rodríguez-Diéguez, D. Choquesillo-Lazarte, C. Martos, J. Á. Botas, F. Martínez and G. Calleja, *ChemPhysChem*, 2019, **20**, 1334–1339.
63 B. Chen, S. Ma, E. J. Hurtado, E. B. Lobkovsky and H. C. Zhou, *Inorg. Chem.*, 2007, **46**, 8490–8492.
64 L. Czepirski and J. JagieŁło, *Chem. Eng. Sci.*, 1989, **44**, 797–801.
65 A. Helal, M. Fettouhi, M. E. Arafat, M. Y. Khan and M. A. Sanhoob, *J. CO_2 Util.*, 2021, **50**, 101603.
66 Y. B. N. Tran, P. T. K. Nguyen, Q. T. Luong and K. D. Nguyen, *Inorg. Chem.*, 2020, **59**, 16747–16759.
67 M. M. Abdelnaby, T. A. Saleh, M. Zeama, M. A. Abdalla, H. M. Ahmed and M. A. Habib, *ACS Omega*, 2022, **7**, 14535–14543.
68 K. Kiatkittipong, M. A. A. Mohamad Shukri, W. Kiatkittipong, J. W. Lim, P. L. Show, M. K. Lam and S. Assabumrungrat, *Processes*, 2020, **8**, 548–569.
69 J. Tapiador, E. García-Rojas, P. Leo, C. Martos, G. Calleja and G. Orcajo, *Microporous Mesoporous Mater.*, 2023, **361**, 112741.
70 J. Tapiador, E. García-Rojas, P. López-Patón, G. Calleja, G. Orcajo, C. Martos and P. Leo, *J. Environ. Chem. Eng.*, 2023, **11**, 109497.
71 T. Lescouet, C. Chizallet and D. Farrusseng, *ChemCatChem*, 2012, **4**, 1725–1728.
72 L. Liu, J. Zhang, H. Fang, L. Chen and C. Y. Su, *Chem.–Asian J.*, 2016, **11**, 2278–2283.
73 T. K. Pal, D. De and P. K. Bharadwaj, *Coord. Chem. Rev.*, 2020, **408**, 213173.
74 Z. Zhou, L. Yang, Y. Wang, C. He, T. Liu and C. Duan, *RSC Adv.*, 2016, **6**, 108010–108016.
75 J. Tapiador, P. Leo, C. Campbell, D. Choquesillo-Lazarte and G. Orcajo, *J. Environ. Chem. Eng.*, 2025, **13**, 119336.
76 J. Tapiador, E. García-Rojas, P. Leo, C. Martos, G. Calleja and G. Orcajo, *Microporous Mesoporous Mater.*, 2023, **361**, 112741.
77 J. Tapiador, P. Leo, A. Rodríguez-Diéguez, D. Choquesillo-Lazarte, G. Calleja and G. Orcajo, *Catal. Today*, 2022, **390–391**, 230–236.
78 B. Parmar, P. Patel, R. S. Pillai, R. I. Kureshy, N. H. Khan and E. Suresh, *J. Mater. Chem. A*, 2019, **7**, 2884–2894.
79 L.-X. You, S.-X. Yao, B.-B. Zhao, G. Xiong, I. Dragutan, V. Dragutan, X.-G. Liu, F. Ding and Y.-G. Sun, *Dalton Trans.*, 2020, **49**, 6368–6376.
80 F. Fei, Y. Dou, X. Hao, W. Lan, Z. Zhou, L. Yang and D. Zhang, *Inorg. Chem. Commun.*, 2019, **106**, 22–26.
81 Y. Tang, W. Chen, R. Liu, L. Wang, Y. Pan, R. Bi, X. Feng, M. He, Q. Chen and Z. Zhang, *ChemistrySelect*, 2021, **6**, 5350–5355.
82 J. Gu, X. Sun, X. Liu, Y. Yuan, H. Shan and Y. Liu, *Inorg. Chem. Front.*, 2020, **7**, 4517–4526.
83 H. Chen, L. Fan, X. Zhang and L. Ma, *ACS Appl. Mater. Interfaces*, 2020, **12**, 27803–27811.
84 N. Sharma, S. S. Dhankhar and C. M. Nagaraja, *Microporous Mesoporous Mater.*, 2019, **280**, 372–378.
85 C. Fang, K. Mao, T. Liu, W. Gong, X. Ji, Z. Li, J. Li, C. Hu, R. Long and Y. Xiong, *CCS Chem.*, 2025, 1–11.
86 R. Erfani-Ghorbani, H. Eshghi and A. Shiri, *RSC Adv.*, 2025, **15**, 7236–7247.
87 CCDC 2391335: Experimental Crystal Structure Determination, 2025, DOI: 10.5517/ccdc.csd.cc2l8cv3.